One Earth

Article

Thermokarst acceleration in Arctic tundra driven by climate change and fire disturbance

Graphical abstract

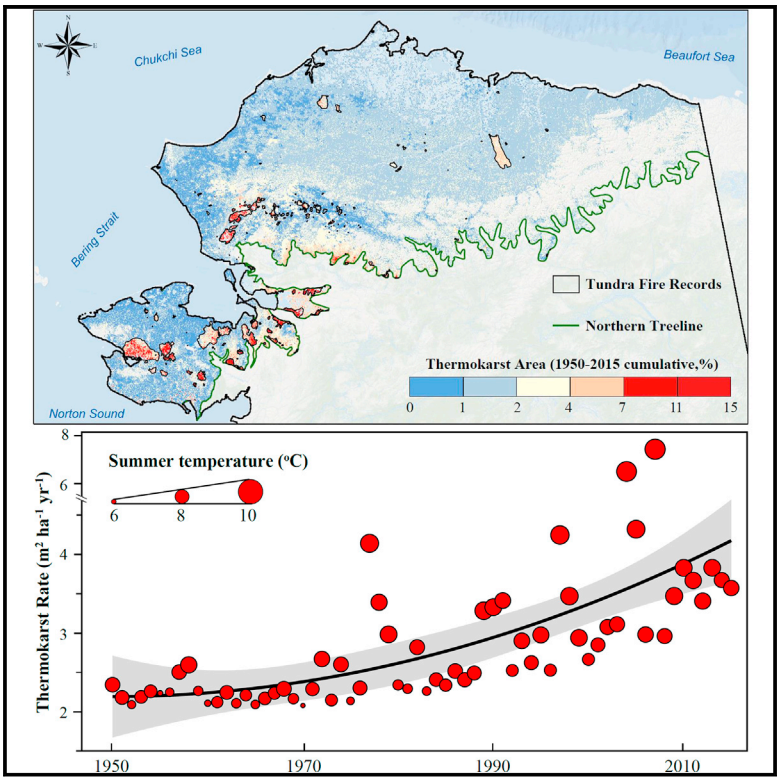

Highlights

- Thermokarst rate has accelerated by a factor of 1.6 since 1950 in Arctic Alaska
- Fire is responsible for 10.5% of all thermokarst formation by burning 3.4% of the area
- Fire has enduring legacy (~8 decades) on thermokarst formation even in low severity

Authors

Yaping Chen, Mark J. Lara, Benjamin M. Jones, Gerald V. Frost, Feng Sheng Hu

Correspondence

ychen@vims.edu (Y.C.), mjlara@illinois.edu (M.J.L.), fshu@wustl.edu (F.S.H.)

In brief

Amplified warming and fire activation in the Arctic pose a growing threat to permafrost thaw. However, current understanding of the synergistic impacts of warming and burning on thermokarst (ground collapse after permafrost thaw) is very limited. Here, we show that thermokarst rates increased by ~60% from 1950 to 2015 in Arctic Alaska, mainly driven by increased summer temperature and prolonged growing season. However, wildfire is disproportionately responsible for 10.5% of all thermokarst formation by burning merely 3.4% of the landscape.

Chen et al., 2021, One Earth *4*, 1–12
December 17, 2021
https://doi.org/10.1016/j.oneear.2021.11.011

CellPress

One Earth

Gold Standard for the Global Goals
3 tons of CO_2 offset

CellPress
OPEN ACCESS

Article

Thermokarst acceleration in Arctic tundra driven by climate change and fire disturbance

Yaping Chen,[1,2,9,*] Mark J. Lara,[1,3,*] Benjamin M. Jones,[4] Gerald V. Frost,[5] and Feng Sheng Hu[1,6,7,8,*]
[1]Department of Plant Biology, University of Illinois at Urbana-Champaign, Urbana, IL 61801, USA
[2]Virginia Institute of Marine Sciences, College of William and Mary, Gloucester Point, VA 23062, USA
[3]Department of Geography, University of Illinois at Urbana-Champaign, Urbana, IL, USA
[4]Institute of Northern Engineering, Water and Environmental Research Center, University of Alaska Fairbanks, Fairbanks, AK 99775, USA
[5]Alaska Biological Research, Inc, P.O. Box 80410, Fairbanks, AK 99708, USA
[6]Department of Geology, University of Illinois at Urbana-Champaign, Urbana, IL 61801, USA
[7]Department of Biology, Washington University in Saint Louis, Saint Louis, MO 63130, USA
[8]Department of Earth and Planetary Sciences, Washington University in Saint Louis, Saint Louis, MO 63130, USA
[9]Lead contact
*Correspondence: ychen@vims.edu (Y.C.), mjlara@illinois.edu (M.J.L.), fshu@wustl.edu (F.S.H.)
https://doi.org/10.1016/j.oneear.2021.11.011

SCIENCE FOR SOCIETY Disruptive permafrost thaw known as thermokarst may propel landscape reorganization and exacerbate high-latitude carbon release. However, current understanding of the thermokarst process remains limited. Here we used a remote sensing dataset unprecedented in spatiotemporal scales and resolutions to characterize regional patterns of thermokarst formation in the ice-rich Arctic tundra ecosystem. Our results show complex thermokarst patterns, intimately regulated by climate change, fire disturbance, and landscape attributes. Though sporadic and short lived, tundra fires have enduring legacy (up to 8 decades) on initiating thermokarst, even with low fire severity. On a regional scale, however, climate warming is the principle factor driving widespread thermokarst acceleration over past decades. As anthropogenic warming and tundra burning intensify in this century, the thermokarst process may emerge as a growing source of uncertainty for the permafrost carbon budget.

SUMMARY

Climate warming is projected to intensify tundra wildfire, with profound implications for permafrost thaw. A major uncertainty is how increased burning will interact with climate change to exacerbate thermokarst (ground-surface collapse resulting from permafrost thaw). Here we show that thermokarst rates increased by ~60% with warming climate and wildfire from 1950 to 2015 in Arctic Alaska. Wildfire amplified thermokarst over 40+ years, cumulatively creating ~9 times thermokarst formation as that in unburned tundra. However, thermokarst triggered by repeat burns did not differ from that triggered by single burns, irrespective of time between fires. Our simulation identified climate change as the principal driver of all thermokarst formed during 1950–2015 (4,700 km^2) in Arctic Alaska, but wildfire was disproportionately responsible for 10.5% of the thermokarst by burning merely 3.4% of the landscape. These results combined suggest that climate change and wildfire will synergistically accelerate thermokarst as the Arctic transitions in this century.

INTRODUCTION

Permafrost underlies ~20% of the Earth's land surface,[1] but it preserves 33% of the global belowground organic carbon pool.[2] Over the past few decades, permafrost degradation has increased coincidentally with rising air temperatures, shifting precipitation regimes, and increased wildfire activity.[3–7] Unlike gradual permafrost thaw (top-down increase in active layer thickness), the abrupt collapse of ice-rich permafrost (i.e., thermokarst) disrupts the entire soil profile, radically altering water, energy, and carbon fluxes.[8–12] Once initiated, thermokarst may proceed without external forces, fueled by a series of positive feedbacks (e.g., altered albedo,[13] snow trapping,[14] and water impoundment[15,16]) to catalyze carbon liberation from deep stockpiles—a process unlikely to reverse under current climatic trends.[17]

Although the potential for thermokarst to exacerbate permafrost carbon feedbacks is well recognized,[12,18] the spatiotemporal patterns, mechanisms, and processes governing thermokarst dynamics are variable across space and poorly understood across

Please cite this article in press as: Chen et al., Thermokarst acceleration in Arctic tundra driven by climate change and fire disturbance, One Earth (2021), https://doi.org/10.1016/j.oneear.2021.11.011

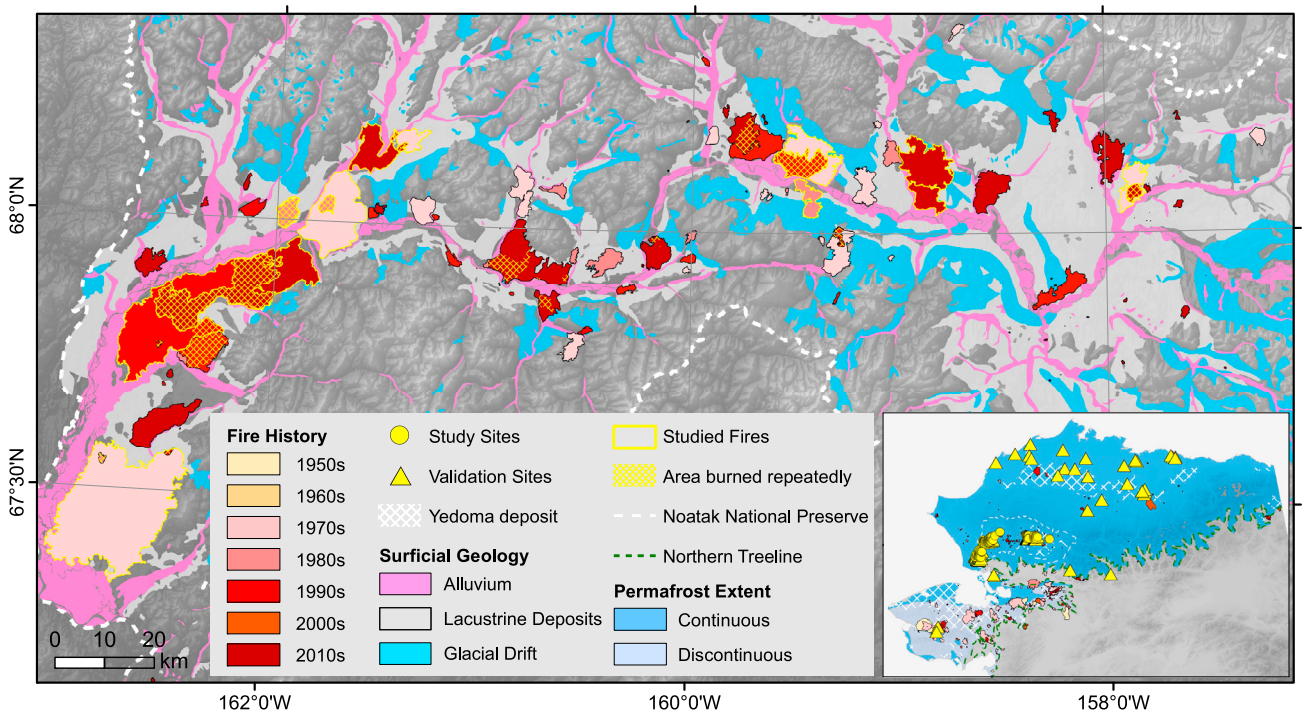

Figure 1. Map of study domain

Sixteen fires (outlined in yellow) occurring between 1971 and 2012 in the NOAT of Arctic Alaska (inserted panel) were studied for thermokarst response to the immediate (2 fires, 318.0 km^2, also see Figure S1), prolonged (2 fires, 481.3 km^2, also see Figure S3), and repeated (12 fires, 164.6 km^2, also see Table S1) impacts of wildfire. Study sites (n = 276, yellow circles) were set up in burned and unburned tundra across different surficial geology types (as proxy of ground ice contents) and gradient of fire severity levels in the NOAT (Figures S1 and S3; Table S1). Yellow triangles (n = 73) indicate data for model validation, derived from literature (n = 14) and our sites in (n = 45) and outside (n = 14) NOAT (Table S3). The maps are superimposed on the GMTED2010 global elevation dataset.[33]

time.[5,15,19] Many interacting factors have been linked with permafrost degradation, including climate,[3,6,20] topography,[21,22] surficial geology,[19,23] ground ice content,[11,24] and fire disturbance.[7,22] Recent evidence from the Anaktuvuk River Fire illuminates the potential influence of tundra fires on permafrost[7,25] and carbon dynamics.[26] For instance, this event triggered expansive thermokarst formation shortly after fire.[7] However, low observation frequencies and rapidly changing environmental conditions have greatly limited our ability to monitor, measure, and model thermokarst-driven landscape evolution across heterogeneous Arctic terrain.

Here we investigated the impact of wildfire, climate change, and landscape attributes on thermokarst dynamics (i.e., fine-scale thermokarst features represented by flooded pits and troughs commonly associated with ice wedge degradation) in Arctic Alaska. We selected the Noatak National Preserve (NOAT, 2.9 × 10^4 km^2) for this study, because this region is among the warmest (mean summer temperature of 10.6°C) and most fire-prone (mean fire return interval of ~400 years) tundra ecosystems on Earth[27,28] and has experienced substantial warming (+2.1°C since 1950)[29] and frequent wildfires over recent decades[30,31] (Figure 1). Thus, the NOAT can be viewed as a bellwether for the Arctic tundra biome if the trend of climate warming and tundra burning continues. We extrapolated the results in the NOAT to the Arctic Alaskan tundra (2.6 × 10^5 km^2) using the Boosted Regression Trees (BRT) machine learning algorithm. Our results reveal widespread thermokarst acceleration in Arctic Alaska during 1950 and 2015, highlighting abrupt thaw as an important avenue of permafrost response to climate change. Remarkably, more than one-tenth of all thermokarst formation was attributable to wildfire, which burned merely ~3% of the tundra landscape. As warming and burning are both predicted to intensify across the pan-Arctic in this century,[32] aggravated thermokarst formation may become a growing source of uncertainty in the feedback of the Arctic ecosystem to the atmosphere. Thus, our results based upon 7 decades of remote sensing observation may provide essential quantitative constraints for earth system models to gain improved confidence in the magnitude of future warming in high latitudes.

RESULTS

Immediate thermokarst response to wildfire

We quantified immediate postfire thermokarst formation across two large recent tundra fires (Uvgoon Creek Fire in 2012 and Sidik Lake Fire in 2010; 318.0 km^2) using the temporally dense commercial satellite images acquired during 2007 and 2015 (Figure S1). We systematically selected the study sites (n = 112) using a stratified random sampling algorithm along gradients of fire severity (high, moderate, low, and unburned) and ground ice content (via surficial geology of alluvium [high], lacustrine deposits [moderate], and glacial drift [low][34,35]) to characterize thermokarst responses to the immediate impacts of wildfires (see experimental procedures and Figure S2).

Please cite this article in press as: Chen et al., Thermokarst acceleration in Arctic tundra driven by climate change and fire disturbance, One Earth (2021), https://doi.org/10.1016/j.oneear.2021.11.011

CellPress
OPEN ACCESS

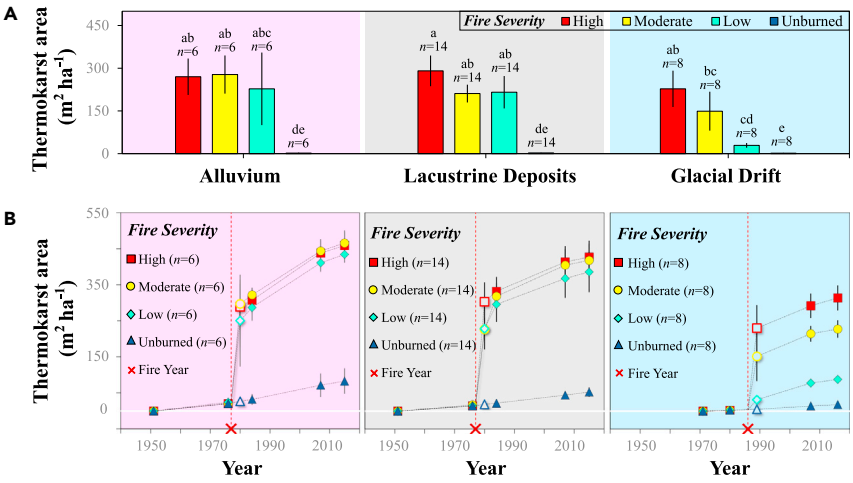

Figure 2. Thermokarst response by fire severity and surficial geology

(A) Immediate impacts of fire disturbance on thermokarst (i.e., pulse thermokarst formation) estimated as the cumulative formation over 3 postfire years. The results were derived from two recently burned tundra (Uvgoon Creek Fire in 2012 and Sidik Lake Fire in 2010) and the surrounding unburned areas (Figure S1). The number of study sites (*n*) is given for each fire severity level × surficial geology type, and different letters indicate significant difference at $p < 0.05$ level.

(B) Long-term thermokarst responses in burned and unburned tundra. The observations were based upon time series of two historical tundra fires (OTZ-NNW38 Fire in 1977 and OTZ-NE100 Fire in 1986) and the adjacent unburned tundra (Figure S3). Solid symbols represent time series of pre- and post-fire thermokarst measurements, while open symbols indicate estimated thermokarst area at 3 years after fire inferred from (A). All data are represented as mean ±1 SE.

Our results suggest that wildfire triggered pulse thermokarst growth (defined as thermokarst formed within 3 years following fire), transforming 213.6 ± 20.6 m^2 ha^{-1} ($n = 84$) of previously undisturbed tundra into thermokarst landforms (Figure 2A). In stark contrast, thermokarst formation within unburned terrain was negligible over the same 3-year period (2.2 ± 0.6 m^2 ha^{-1}, $n = 28$; Figure 2A). The pulse of thermokarst was significantly higher ($p < 0.001$) in the ice-rich, poorly drained lowland alluvium (258.5 ± 49.6 m^2 ha^{-1}, $n = 18$) and lacustrine deposits (239.1 ± 28.0 m^2 ha^{-1}, $n = 42$) than the relatively well-drained upland glacial drift (135.3 ± 34.4 m^2 ha^{-1}, $n = 24$) (Figure 2A). Fire severity did not appear to influence thermokarst formation in alluvium or lacustrine deposits ($p > 0.9$; Figure 2A), whereas in glacial drift, thermokarst was ~7 times greater in high-severity (227.6 ± 63.7 m^2 ha^{-1}, $n = 8$) than in low-severity (29.1 ± 8.2 m^2 ha^{-1}, $n = 8$) burns (Figure 2A).

Long-term thermokarst patterns

We used an extensive compilation of historical and contemporary images acquired during 1951 and 2016 to continuously monitor thermokarst patterns across unburned and burned tundra (OTZ-NNW38 Fire in 1977 and OTZ-NE100 Fire in 1986; 481.3 km^2) (see experimental procedures and Figure S3). The time series of unburned tundra ($n = 28$) revealed widespread thermokarst acceleration with recent warming in the NOAT (Figures 2 and 3; Table 1). The greatest increase in thermokarst rates appeared in alluvium (by 275.3% ± 156.7% from 1951 to 1976 to 1977 to 2015, $n = 6$), followed by lacustrine deposits (by 85.5% ± 24.9% from 1951 to 1976 to 1977 to 2015, $n = 14$) and glacial drift (by 47.6% ± 15.7% from 1971 to 1980 to 1981 to 2016, $n = 8$) (Table 1; Figure 2B).

Fire disturbance magnified thermokarst rates throughout the monitored 38 postfire years (Table 1), cumulatively creating ~9 times the amount of thermokarst formation (406.0 ± 20.0 m^2 ha^{-1}, $n = 60$) as would be expected without fire (45.2 ± 9.9 m^2 ha^{-1}, $n = 20$) (Figure 2B). Thermokarst rates in burned tundra ($n = 84$) were significantly higher ($p < 0.05$) than those in unburned tundra ($n = 28$) during our postfire observation regardless of fire severity and surficial geology (Table 1). Notably, more than half of the observed thermokarst formation appeared within the first postfire decade, after which thermokarst rates dwindled precipitously (Table 1; Figure 3). Postfire thermokarst rates reached 22.4–177.1 times that of unburned tundra during the first decade and drastically declined during the second and third decades (2.6–10.1) but remained 1.6–2.1 times that of unburned tundra by the end of the fourth decade (Table 1; Figure S4). We estimated the time required for thermokarst rates in burned tundra to return to that of unburned tundra to be 51, 47, and 80 years for alluvium, lacustrine deposits, and glacial drift, respectively (see Figure S4).

Long-term thermokarst formation was spatially and temporally variable, manifested as asynchronous thermokarst onsets, diverse geomorphological expressions (or thermokarst modes[23]), and differential responses to fire severity (Figure 3). Prior to fire occurrence in the 1970s, thermokarst features were already prevalent in lowland alluvium and lacustrine deposits, but largely absent in upland glacial drift (Figures 2B and 3). Three decades after fire, thermokarst features existed primarily in the form of degraded permafrost plateaus in alluvium, interconnected trough networks in lacustrine deposits, and discrete flooded pits or ponds in glacial drift (Figure 3). Consistent with pulse thermokarst responses, long-term thermokarst response in burned alluvium and lacustrine deposits showed no differences between fire severity levels ($p > 0.87$), whereas emerging thermokarst in glacial drift was largely concentrated in severely burned areas (Figures 2B and 3). Unlike lowland alluvium or lacustrine deposits where the prevalence of flow paths (conducive to surface water exchange) may homogenize thermokarst formation across uneven burns,[37] thermokarst features initiated by severe burns in upland glacial drift were relatively isolated, serving as hotspots for thermokarst expansion over decades following fire (Figure 3).

Impact of repeat burns

To determine if thermokarst response to a subsequent burn differs from that of an initial burn, we studied thermokarst formation in six areas (164.6 km^2) burned twice by 12 fires during 1971 and

Please cite this article in press as: Chen et al., Thermokarst acceleration in Arctic tundra driven by climate change and fire disturbance, One Earth (2021), https://doi.org/10.1016/j.oneear.2021.11.011

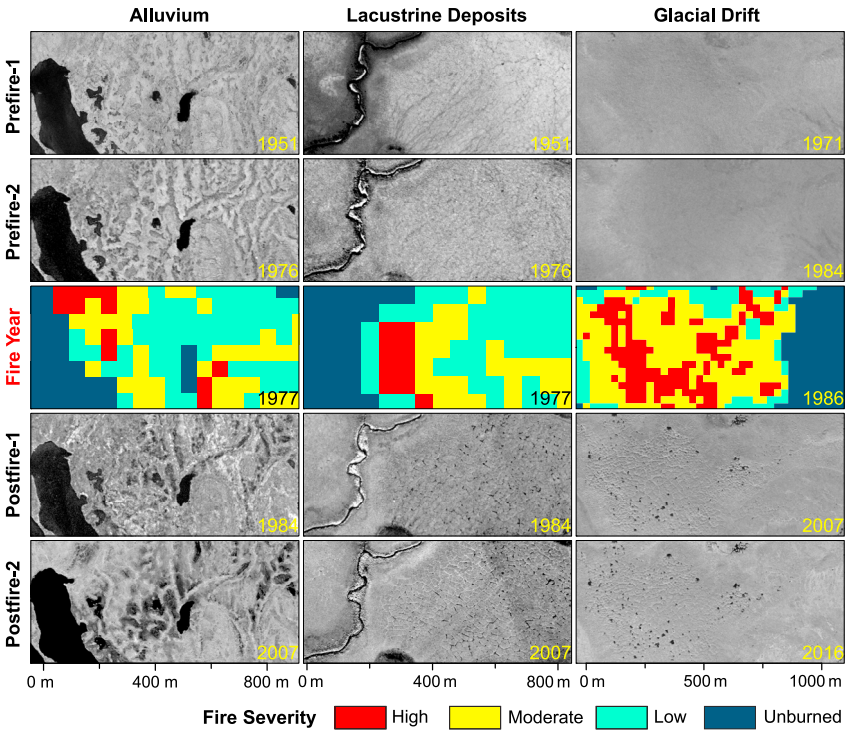

Figure 3. Spatiotemporal heterogeneity of thermokarst formation in burned and unburned tundra

The aerial and satellite images were presented in time series (columns) by surficial geology types at 1-m resolution. The demonstration sites of alluvium and lacustrine deposits are located within the OTZ-NNW38 Fire burning in 1977, and the demonstration site of glacial drift is from the OTZ-NE100 Fire occurring in 1986 (Figure S3). The fire severity map of the 1986 OTZ-NE100 Fire is obtained from the MTBS data archive, computed by dNBR (https://www.mtbs.gov/). Fire severity information of the relatively old 1977 OTZ-NNW38 Fire is unavailable from the MTBS archive and was computed with dGEMI, an alternative fire severity index to dNBR.[36]

2012 (Figure 4; Table S1). All the fires were selected from lacustrine deposits (see experimental procedures) with the time between overlapping burns spanning from 6 to 38 years (Table S1). Due to lack of early images for direct measurements of thermokarst immediately after fire, we retrogressively computed pulse thermokarst formation associated with each fire using three scenarios (Figure S5). Scenario 1 assumed that thermokarst rate following the first fire was unaffected by the occurrence of the second fire and continued to decrease over time. Alternatively, scenario 2 assumed that the impact of the first fire ended by the occurrence of the second fire, which took its turn to dictate thermokarst rate. Scenario 3 assumed that the first and the second fires contributed additively to driving thermokarst rates (Figure S5). Using the thermokarst rates generated earlier (Table 1; Figure S4) and the thermokarst areas measured before the first fire, between the first and the second fire, and after both fires (Figure S5), we estimated the pulse thermokarst formation following the second fire to be 270.1 ± 15.5, 214.5 ± 16.0, and 200.0 ± 16.3 m^2 ha^{-1} (n = 52) for scenarios 1, 2, and 3, respectively (Figure 4). Regardless of scenarios, the amount of thermokarst triggered by the second fires did not differ from that by the first fires (201.8 ± 17.9 m^2 ha^{-1}, n = 52, $p > 0.2$), nor did it differ with time since last burn ($R^2 < 0.01$, $p > 0.48$; Figure 4).

Modeling regional thermokarst dynamics

We pooled the thermokarst data in burned and unburned tundra (Figure 2; Table 1) to model rates of thermokarst with potential environmental drivers (e.g., temperature, precipitation, and topography; Table S2) using the BRT machine learning algorithm. Our model explained 73% of the variance in thermokarst rates (10-CV = 0.69 ± 0.01, $p < 0.001$) with six variables: year since fire (YSF), mean summer air temperature (MSAT), length of growing season (LOGS), full snow season duration (FSS), permafrost probability (PP), and topographic position (TPI) (Figures S6 and S7). We then applied the model to simulate annual thermokarst rate of each 1 km^2 tundra of Arctic Alaska during 1950–2015 (Figure 5 and Figure S8), and the results were validated (R^2 = 0.7, $p < 0.001$) by field and remote sensing observations from a range of burned and unburned tundra ecosystems, including the Arctic Coastal Plain (e.g., Prudhoe Bay[19,38]), Brooks Range Foothills (e.g., 2007 Anaktuvuk River Fire), Brooks Range (e.g., 1977 BTTW47 Fire), and Seward Peninsula (e.g., 1954 Imuruk Basin Fire) (Figure S7; Table S3).

Model simulations illustrated that thermokarst area increased considerably during 1950–2015 in Arctic Alaskan tundra (Figure 5; Video S1). The rate of thermokarst formation grew by a factor of 1.6 from 1950 (2.3 ± 0.05 m^2 ha^{-1} $decade^{-1}$) to 2015 (3.7 ± 0.07 m^2 ha^{-1} $decade^{-1}$), and thermokarst area increased by 4,655 km^2, or ~2% of all modeled area since 1950 (Figure 5). We identified the relative contributions of fire disturbance (10.5%) to regional thermokarst formation (see experimental procedures), and found that climate change (e.g., increase of MSAT and LOGS) accelerated thermokarst after the late 1970s, and that wildfires reinforced this trend by amplifying thermokarst, especially during high-fire years (e.g., 1977, 2007) (Figure 5). Substantial spatial variability exists across tundra ecoregions, generally mirroring latitudinal gradients of climate and fire regimes (Figure 5 and Figure S8). For instance, in the relatively cold Arctic Coastal Plain (the northmost ecoregion), only 0.6% of the land surface transitioned to thermokarst landform during 1950–2015 with minimal contribution from

Please cite this article in press as: Chen et al., Thermokarst acceleration in Arctic tundra driven by climate change and fire disturbance, One Earth (2021), https://doi.org/10.1016/j.oneear.2021.11.011

Table 1. Time series of thermokarst rate (m^2 ha^{-1} $year^{-1}$) in burned and unburned tundra

			Burned			
Surficial geology	Time span	Unburned	Low fire severity	Moderate fire severity	High fire severity	Overall
Alluvium	1951 ~ 1976	0.8 ± 0.5				
	1977 ~ 1980	1.4 ± 0.5	76.6 ± 42.5	93.3 ± 22.3	90.8 ± 21.3	86.9 ± 16.5
	1981 ~ 1984	1.4 ± 0.5	14.3 ± 6.2	8.6 ± 3.7	10.8 ± 5.6	11.2 ± 2.9
	1985 ~ 2007	1.7 ± 0.8	5.4 ± 0.7	5.3 ± 0.9	5.7 ± 0.4	5.5 ± 0.4
	2008 ~ 2015	1.4 ± 0.4	2.9 ± 0.5	2.7 ± 0.5	2.7 ± 0.5	2.8 ± 0.3
Lacustrine deposits	1951 ~ 1976	0.6 ± 0.1				
	1977 ~ 1980	0.9 ± 0.3	71.9 ± 18.9	70.4 ± 10.4	96.9 ± 18.0	79.7 ± 9.3
	1981 ~ 1984	0.9 ± 0.3	22.9 ± 11.0	27.4 ± 7.9	16.3 ± 7.9	22.2 ± 5.2
	1985 ~ 2007	1.0 ± 0.2	3.1 ± 0.5	3.8 ± 0.5	3.5 ± 0.4	3.5 ± 0.3
	2008 ~ 2015	1.1 ± 0.3	2.2 ± 0.5	1.7 ± 0.2	1.8 ± 0.1	1.9 ± 0.2
Glacial Drift	1971 ~ 1985	0.3 ± 0.1				
	1986 ~ 1989	0.4 ± 0.1	9.6 ± 2.7	49.6 ± 22.8	75.8 ± 21.2	45.0 ± 11.5
	1990 ~ 2007	0.4 ± 0.1	2.7 ± 0.5	3.9 ± 1.2	4.3 ± 1.7	3.7 ± 0.7
	2008 ~ 2016	0.4 ± 0.1	1.1 ± 0.3	1.5 ± 0.4	2.4 ± 0.3	1.7 ± 0.2

The thermokarst rates presented here are converted from thermokarst area (m^2 ha^{-1}), based on immediate and long-term thermokarst observations in burned and unburned tundra, as presented in Figure 2.
The thermokarst rate between two time points is computed as differenced thermokarst area divided by the years in between (Figure S2).
The "*Overall*" column in burned tundra represents thermokarst rate averaged across all burned sites from low, moderate, and high fire severity.
All values are shown as mean ±1 SE.

wildfire (0.03%) (Figure S8). Meanwhile in Seward Peninsula (the southernmost ecoregion), 3.1% of the land surface degraded, in which fire is responsible for 32.9% of the thermokarst formation (Figure S8).

DISCUSSION

Nearly 70 years of aerial and spaceborne observations uncovered dynamic spatiotemporal patterns of permafrost degradation in response to climate change and fire disturbance in Arctic Alaska (Video S1). The finding that wildfire contributed to one-tenth of thermokarst growth is striking given limited spatial extent of historical tundra fires in the Arctic.[28] Nonetheless, climate change remains the dominant force driving widespread acceleration of thermokarst across contemporary tundra landscape.

Thermokarst rates in unburned NOAT progressively increased over recent decades (Table 1). In the absence of fire, thermokarst rates ranged between 4.0 and 12.9 m^2 ha^{-1} $decade^{-1}$ in the NOAT, comparable to those observed in other unburned tundra ecoregions of Alaska, such as Arctic Coastal Plain (1.2–34.9 m^2 ha^{-1} $decade^{-1}$),[19] Brooks Range Foothills (12.1 m^2 ha^{-1} $decade^{-1}$), Brooks Range (2.1 m^2 ha^{-1} $decade^{-1}$), Kotzebue Lowlands (15.8 m^2 ha^{-1} $decade^{-1}$), and northern Seward Peninsula (7.6 m^2 ha^{-1} $decade^{-1}$) (Figure S7). However, these rates were substantially lower than those reported in the heavily industrialized areas near Prudhoe Bay, which reached up to 32.8–155.7 m^2 ha^{-1} $decade^{-1}$ [3,17,36]. Therefore, the thermokarst response captured in our unburned sites represented many undisturbed tundra ecosystems well, as confirmed by the model outputs across Arctic Alaska ($R^2 = 0.7$, $p < 0.001$). Although gradual thermokarst acceleration seemed to be the norm across tundra ecosystems, fire disturbance created local hotspots of excess thermokarst formation.

Tundra fires increased the vulnerability of land surface to thermokarst formation. Fires only burned ~3% of the area in Arctic Alaska since 1950 but were responsible for more than 10% of all thermokarst formation. The pulse thermokarst growth triggered shortly after fire was likely in response to the abrupt shift in surface energy balance, as albedo decreases with charred ground[39] and thermal insulation weakens after organic soil removal.[30,40] The modified environmental conditions change subsurface permeability and microtopography associated with thaw settlement and facilitate surface water impoundment. Surface water is low in albedo and high in thermal conductivity that enhances heat trapping and heat propagation in frozen soils,[13,41] which feeds positively back to thermokarst expansion that disproportionately affects ice-rich, poorly drained tundra lowlands (i.e., alluvium and lacustrine deposits). Nonetheless, thermokarst rates in burned tundra quickly decreased after the first decade (Table 1), similar to the pattern observed in boreal forests following postfire vegetation recovery.[42] Unlike the 2–3 decades needed for thermokarst to stabilize in burned boreal forests,[42] however, thermokarst rates in burned tundra may remain elevated for 5–8 decades before returning to those in unburned tundra (Figure S4).

After analyzing all available images acquired across NOAT, one of the most fire-prone tundra ecosystems on earth,[28] we did not find evidence linking repeat burns with intensified thermokarst response. This result is surprising given the relatively short period between the observed first and second fires (6–38 years) to the mean fire return interval of NOAT (~400 years).[30] Although repeat burns still produced a pulse of thermokarst, the amount was not statistically different from that of a single

Please cite this article in press as: Chen et al., Thermokarst acceleration in Arctic tundra driven by climate change and fire disturbance, One Earth (2021), https://doi.org/10.1016/j.oneear.2021.11.011

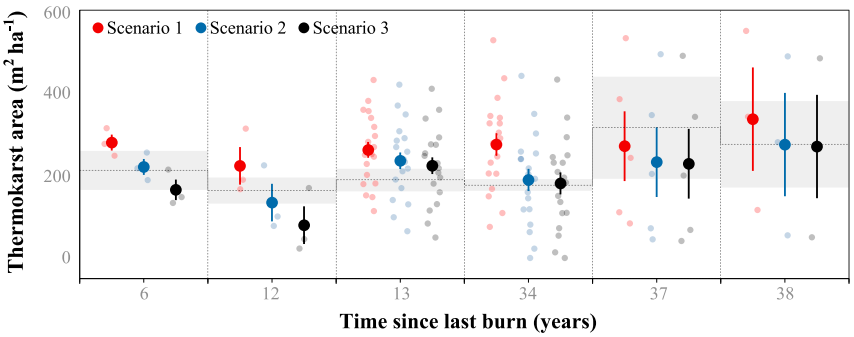

Figure 4. Thermokarst response to repeat burn

The results were generated from six areas (separated by the dotted vertical lines) that have been burned twice since 1950 (a total of 12 fires) in lacustrine deposits (Table S1). The time between the initial and the subsequent burns ranged from 6 to 38 years (*x* axis). The shaded area (mean ±1 SE) refers to pulse thermokarst formation (m^2 ha^{-1}) associated with the initial burn (see Equation 1 and Figure S5). The pulse thermokarst formation (m^2 ha^{-1}) caused by the repeat burns was computed with three scenarios (Equation 2; Figure S5) differentiated by colors. The transparent circles represent individual observations, and the solid circles are mean (±1 SE). Scenario 1 (red) assumed that thermokarst rate following the initial burn was unaffected by the occurrence of the subsequent burn and continued to decrease over time. Alternatively, scenario 2 (blue) assumed that the impact of the initial burn ended by the occurrence of the subsequent burn, which took its turn to dictate thermokarst rate. Scenario 3 (black) is the sum of scenarios 1 and 2, assuming that both fires contributed additively to thermokarst rates (Figure S5).

burn. Several mechanisms may be involved to explain this *insensitivity* of tundra to repeat burns, including (1) insulative vegetation may have rapidly recovered following fire that restores soil thermal regime and buffers permafrost from ambient environments,[43] (2) plant species and the associated fuel types may have shifted toward a fire-resistant community,[44] and (3) soil moisture may have been altered by the reorganization of drainage networks that prevent returning fires from burning into deep horizons (Figure 3). The potential suppression of repeat burns was evidenced by our observations, as we found that the second burns tended to be less severe than the first burns (Table S1). Further interpretation of these results should be made with caution as minimal area of tundra has experienced repeat burns in the past (<0.1% of Arctic Alaska, 1950–2020).[31]

These findings, together with our model simulations, outline a general pattern of regional thermokarst propagation, characterized by gradual but pervasive thermokarst acceleration driven by climate warming, punctuated by periods of pronounced but localized thermokarst aggravation forced by fire. Assuming a space-for-time substitution, the tundra ecoregions of northern Alaska may represent a range of possible future states of climate and fire regimes in the tundra biome. Our model simulations suggest that the relatively warm and fire-prone southern ecoregions (e.g., Seward Peninsula and Kotzebue Sound Lowlands) have substantially more thermokarst formation than the northern ecoregions (e.g., Arctic Coastal Plain, Brooks Range Foothills, Brooks Range), in which fire was responsible for one-third of the formation (the difference between the fireRun and the nofireRun) in these southern ecoregions (Figure S8). With amplified warming in high latitudes,[45] similar conditions will likely develop in the north. The northern tundra regions may be especially primed for rapid thermokarst progression, where massive ice close to the ground surface[46] has slowly developed over a millennial timescale in the absence of fires.[28] The heightened vulnerability of northern regions to activating wildfire was well exemplified by the Anaktuvuk River Fire (in the Brooks Range Foothills), where over one-third of burned area formed thermokarst after 7 years.[7]

The Arctic landscape is in rapid transition. This study showcases the synergistic impact of climate change and fire disturbance on abrupt permafrost degradation on decadal to centennial timescales—a process unlikely to be captured by short-term observations. Although the response of permafrost landscapes to wildfire is dependent on permafrost properties and geomorphology,[47–49] our results derived from various environmental contexts are informative for many areas of the circumpolar Arctic, such as the Beringian landscapes of Alaska and Siberia, which have recently experienced an unusually prolific fire season.[50] Considering the enduring efficacy of wildfire in provoking thermokarst and the projected fire activation across the pan-Arctic,[32] the significance of tundra fires in determining future permafrost extent and content may continue to grow.

It is worth noting that the thermokarst patterns studied here only focused on fine-scale thermokarst features commonly associated with ice wedge degradation. We did not include meso-scale thermokarst or thermoerosional features such as retrogressive thaw slumps, active layer detachment slides, coastal bluff erosion, or thermokarst lake dynamics, all of which show signs of intensification with climate change.[6,51–55] Since permafrost serves as the physical foundation buttressing the Arctic landscape, its collapse has cascading impacts on myriad ecosystem properties and functions.[9,37,56,57] As we continue to gain insights into the controls and patterns on past and present permafrost dynamics, the significance of such landscape evolutionary processes on biogeochemical and biophysical feedbacks should emerge as a research priority.[5,58] As such, these datasets will provide essential quantitative constraints for benchmarking elusive thermokarst processes in terrestrial and earth system models[59] for improved understanding of regional to pan-Arctic terrestrial-atmosphere feedbacks.

EXPERIMENTAL PROCEDURES

Resource availability

Lead contact

Further information and requests for resources should be directed to and will be fulfilled by the lead contact, Yaping Chen (ychen410@illinois.edu).

Materials availability

This study did not generate new, unique materials.

Data and code availability

All data have been deposited at NSF Arctic Data Center (https://arcticdata.io/catalog/view/doi%3A10.18739%2FA2610VT0G) and are publicly available as of the date of publication. This paper does not report original code. Any

Please cite this article in press as: Chen et al., Thermokarst acceleration in Arctic tundra driven by climate change and fire disturbance, One Earth (2021), https://doi.org/10.1016/j.oneear.2021.11.011

CellPress
OPEN ACCESS

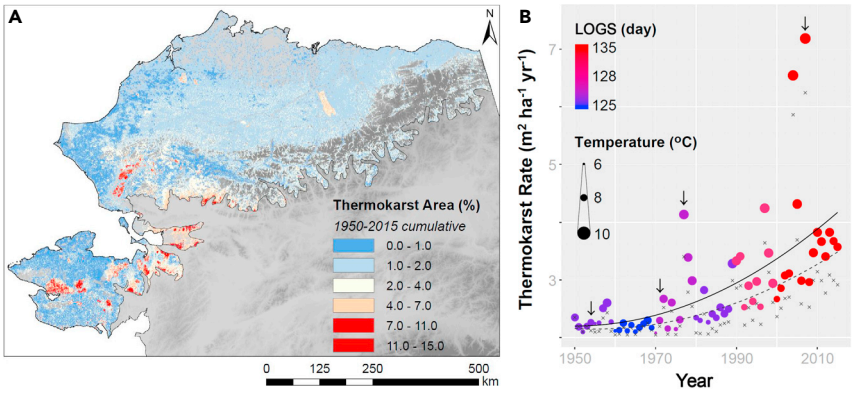

Figure 5. Regional thermokarst formation during 1950 and 2015 in Arctic Alaskan tundra

(A) Cumulative thermokarst formation (1950–2015) of each 1-km^2 pixel across the 2.6 × 10^5 km^2 northern Alaskan tundra (excluding lakes, glaciers, ice sheets, and barren lands). The result is based upon model output forced with historical fires (i.e., fireRun; see Figure S8 for results of individual tundra ecoregion).

(B) Annual thermokarst rate of paired model runs forced with historical fires (colored dots, fireRun) and without historical fires (black crosses, nofireRun) (Figure S8). The solid and dotted lines correspond to linear regression of annual output of fireRun and nofireRun, respectively. The arrows point out 4 extreme tundra fire years when annual area burn exceeds 95% quantile range of tundra fire records (1950–2015). LOGS, length of growing season. Temperature, mean summer area temperature. More information of model simulation and validation can be found in Figures S6–S8.

additional information required to reanalyze the data reported in this paper is available from the lead contact upon request.

Study site

The Noatak National Preserve (NOAT) is located in northwestern Alaska (Figure 1). This region has a relatively warm climate with mean growing season temperature of 10.6°C and total growing season precipitation of 108.3 mm (data from the nearest meteorological station at the Kotzebue Airport, https://www.ncdc.noaa.gov/, 1980–2020). The NOAT has experienced frequent burning over past decades, with an estimated mean fire return interval (FRI) around 400 years[30]. The majority of the vegetated area (dominated by shrub-tussock tundra[60]) in the NOAT is characterized by surficial geological substrates of alluvium (including alluvial deposits, eolian sand, silt and organic deposits, and terrace deposits), lacustrine deposits (lacustrine, glaciolacustrine, and glacial-marine deposits), and glacial drift (glacial and ice-contact gravel deposits),[34] generally corresponding to ground ice contents from high to low.[21,35,61]

The alluvium in the NOAT was deposited during the Holocene and Pleistocene, spatially restricted to valleys and lowland basins associated with terraces and floodplains dissected by streams and rivers.[34] The terrain of alluvium is relatively smooth, and the sediments are normally featured by sandy silt or organic-rich silt that contains massive segregated ice or ice wedges.[35,62] Lacustrine deposits are expansive in the NOAT, formed during the Holocene and Pleistocene with small areas during the late Tertiary.[34] Lacustrine deposits are largely characterized by fine-grained sediments containing abundant ice as lenses and wedges, normally occupying thaw basins including glacial and non-glacial lakes in peaty lowlands.[62] Glacial drift was deposited either directly by glacial ice or by meltwater during the Holocene and late Pleistocene, usually found in upland and hillslope tundra in the NOAT.[34] The terrain of glacial drift, frequently interspersed with kittle lakes, contains ice of various volume.[62] Despite the presence of colluvial deposits (mass wasting and lower slope deposits in hilly terrain) within the NOAT, we did not include it due to its low ground ice content and limited distribution in vegetated tundra of northern Alaska.[34,35]

Image acquisition and preprocessing

We acquired 542 high-quality optical images (resolution of 0.2–1.5 m) spanning the period of 1951–2018 to study thermokarst dynamics across time and space. All images were acquired during the snow-free season, in which 12%, 49%, 28%, and 11% of the images were in June, July, August, and September, respectively. These aerial and satellite images were obtained from three data sources: 287 aerial photographs acquired between 1951 and 2007 by NASA AMES Research Center and NASA Johnson Space, 172 declassified military intelligence photographs acquired between 1972 and 1984 by the Keyhole satellite system KH, and 83 commercial satellite images acquired between 2000 and 2018 from Polar Geospatial Center (satellites: Quickbird-2, Worldview-1, Worldview-2, Worldview-3, Ikonos, Geoeye-1, and OrbView-3). Image orthorectification and co-registration were performed following standard protocols given by Necsoiu et al.[63] 93.3% of the images have a ground resolution between 0.2 and 1.0 m, and the remaining have a resolution between 1.1 and 1.5 m. The small differences in resolution do not affect the clarity to which fine-scale thermokarst features can be identified and measured. The overall registration root-mean-square error is less than 1.0 m (median of 0.22 m, range between 0.001 and 0.66 m).

Uncertainty analysis of thermokarst detection

Our thermokarst detection is largely based upon directional changes of waterlogged features (e.g., flooded pits, ponds, and troughs; Figure S2).[19,64] To ensure that the results are not an artifact arising from intra-annual surface water fluctuation (due to factors such as precipitation or spring runoff),[19,64] we assessed monthly surface water extent from June to September (i.e., growing season) (Figure S9). Images used for the analysis were acquired in four years (2008, 2010, 2013, and 2016) that differed in monthly precipitation patterns (NOAA, https://www.ncdc.noaa.gov/). We set up 35 study sites (500 by 500 m) across alluvium (n = 7), lacustrine deposits (n = 17), and glacial drift (n = 11) (Figure S9). Within each surficial geology type, we placed the study sites along topographic gradients to account for variable drainage conditions and water retention capacities (Figure S9).

Our analysis revealed that monthly surface water extent within thermokarst features oscillated minimally from June to September (Figure S9; Table S4). Surface water extent was relatively stable between July and August (peak growing season, 2.1 ± 0.7 m^2 ha^{-1}, n = 35), but slightly increased between June and September (5.2 ± 1.7 m^2 ha^{-1}, n = 35; Table S4). This monthly pattern was consistent across the landscape, as reflected in lowland alluvium (5.6 ± 0.8 m^2 ha^{-1}, n = 7), lacustrine deposits (3.7 ± 1.1 m^2 ha^{-1}, n = 17), and upland glacial drift (2.1 ± 0.6 m^2 ha^{-1}, n = 11; Table S4), collectively suggesting negligible influence of surface water fluctuation on our interpretation of thermokarst time series.

Quantifying immediate impact of fire

We monitored thermokarst dynamics within the first 3 years after fire (i.e., pulse thermokarst formation). The 3-year time span is constrained by image availability and postfire charcoal persistence.[65] We selected fires across NOAT for this study according to three criteria: (1) they encompass different levels of fire severity (high, moderate, and low), (2) they span a gradient of ground ice contents (alluvium, lacustrine deposits, and glacial drift), and (3) they have both prefire ($\leq$3 years before fire) and postfire (at 3 years after fire) images available. The fires fulfilling these requirements are the Uvgoon Creek Fire in 2012 and the Sidik Lake Fire in 2010 (Figure S1).

Please cite this article in press as: Chen et al., Thermokarst acceleration in Arctic tundra driven by climate change and fire disturbance, One Earth (2021), https://doi.org/10.1016/j.oneear.2021.11.011

The Uvgoon Creek Fire occurred in the summer of 2012, burning an area of 217.2 km^2 with 8.4, 151. 8, and 16.9 km^2 in alluvium, lacustrine deposits, and glacial drift, respectively (Figure S1). Within the fire perimeters, 26.3%, 47.5%, and 15.2% of the area was respectively classified as high, moderate, and low fire severity (Monitoring Trends in Burn Severity, MTBS, https://www.mtbs.gov/). The Sidik Lake Fire (100.8 km^2) occurred in the summer of 2010 (Figure S1). The fire burned across alluvium (10.4 km^2), lacustrine deposits (60.6 km^2), and glacial drift (20.2 km^2), predominantly in low to moderate fire severity (2.2%, 22.8%, and 48.4% high, moderate, and low, respectively).

To separate fire-induced thermokarst from background changes, we created two zones (radius of 500 and 2000 m) around the fire perimeters (Figure S1). The 500-m zone serves as the transition between burned and unburned tundra, and the region between 500 and 2000 m was used as the unburned area for comparison with the adjacent burn. We set up 112 study sites (500 × 500 m each) using stratified random sampling to ensure unbiased representation of fire severity and surficial geology type (Figure S1). The number of study sites assigned to each surficial geology type was proportional to its surface area in the NOAT: alluvium (21%, $n = 24$), lacustrine deposits (50%, $n = 56$), and glacial drift (29%, $n = 32$). Within each surficial geology type, an even number of study sites was assigned among unburned, low, moderate, and high severity area.

We quantified thermokarst area in each study site both before and after fire using manual delineation.[66,67] Although troughs (i.e., typical features of polygonal tundra associated with ice wedge degradation, formed by the alternating thermal expansion and contraction) are easily identifiable in high-resolution images, manually digitizing trough area is challenging and may introduce unintended errors given their abundance and relatively small size (Figure S2). Developing troughs grow in size, shown as increase in length, width, and connectivity in optical images over time. Therefore, we used *Polyline* (in ArcGIS 10.5) to outline the well-defined trough centers, and we generated buffers with a given distance (range of 0.5–1.5 m) to approximate trough area (Figure S2). The buffer diameter was determined for each study as the average width of a sample of 20–30 randomly selected troughs within each site. For features that were initially flooded but drained at a later period (e.g., pits and troughs), they were still counted (not removed) as thermokarst area given that the loss of ground ice is unlikely to rapidly restore under current climatic conditions.[11,17] All results were normalized to square meter per hectare (m^2 ha^{-1}). The pulse thermokarst formation was then computed as the difference between areas quantified before and after fire. All geoprocessing was completed in ArcGIS 10.5 at the spatial scale of 1:3,000.

Quantifying long-term impact of fire

We studied multidecadal-scale thermokarst dynamics across two of the oldest fires observed in the NOAT (the OTZ-NNW38 Fire in 1977 and the OTZ-NE100 Fire in 1986[31]). These fires were selected following similar criteria given above, i.e., fire severity, surficial geology, and image availability. In a similar fashion, all unburned sites were located within an area between 500 and 2000 m radius surrounding the fires (Figure S3).

The OTZ-NNW38 Fire occurred in 1977, burning an area of 459.5 km^2 across alluvium and lacustrine deposits (Figure S3). It represented the fourth largest tundra fire ever recorded north of the Arctic circle.[36] The area burned in high, moderate, and low severity respectively accounted for 12.9%, 45.8%, and 41.3% (Figure S3).[36] There were five years with full imagery coverage of this area, and they are 1951 and 1976 (prefire) and 1984, 2007, and 2015 (postfire). The OTZ-NE100 Fire (21.8 km^2) took place in 1986 in glacial drift. It burned 45.7%, 38.9%, and 15.4% of the area in low, moderate, and high severity, respectively (Figure S3). The years with full imagery coverage of the OTZ-NE100 Fire are 1971 and 1980 (prefire) and 2007 and 2016 (postfire).

We set up 112 study sites (500 × 500 m each) across these fires following the same stratified random sampling protocol as described above (Figure S3). The thermokarst area (m^2 ha^{-1}) in each study site was repeatedly measured using manual delineation (Figure S2), and the rate of thermokarst (m^2 ha^{-1} $year^{-1}$) within any given time interval was calculated as differenced thermokarst area divided by the number of years in between (Figure S2).

Quantifying impact of repeat burns

A total area of 333.5 km^2 in the NOAT was burned repeatedly (no more than twice) over the past ~70 years by 35 fires, with the time between the initial and the subsequent fires ranging from 6 to 38 years.[31] The majority of repeat burns (266.8 km^2) fall within the most extensive surface geology of lacustrine deposits in the NOAT (Figure 1). Alluvium and glacial drift combined account for ~6% of the area burned repeatedly. As a result, our study of repeat burns was only conducted on lacustrine deposits (Table S1).

To compare the amount of pulse thermokarst formation associated with an initial burn (at time T_{F_1}) and a repeat burn (at time T_{F_2}), images acquired at the time before burns (T_1), between burns (T_2), and after burns (T_3) were needed (Figure S5). This requirement was met by 12 fires in six locations, with an overlapping burned area of 216.4 km^2 (Table S1). We set up a total of 52 study sites (500 × 500 m each) in the six repeatedly burned locations. The number of sites assigned to each location is proportional to its area, and each location has a minimum of three sites (Table S1). We quantified thermokarst area within each study site at T_1, T_2, and T_3 (Figure S5) using the same approach outlined above (Figure S2). The pulse of thermokarst formed by the initial burn (TK_{F_1}, m^2 ha^{-1}) was computed as follows:

$$TK_{F_1} = TK_{T_2} - TK_{T_1} - \int_{T_1}^{T_{F_1}} f_1(t)dt - \int_{T_{F_1}+3}^{T_2} f_2(t)dt \qquad \text{(Equation 1)}$$

where TK_{T_1} and TK_{T_2} correspond to the thermokarst area measured at T_1 and T_2, respectively (Figure S5). f_1(t) and f_2(t) refer to the thermokarst rates between T_1 and the initial burn, and between the initial burn and T_2. These rates are a function of time (unit: year), generated from our above described thermokarst rates observed across unburned and burned tundra (Table 1; Figure S4).

Similarly, the pulse thermokarst formation by the repeat burn (TK_{F_2}, m^2 ha^{-1}) was calculated as follows:

$$TK_{F_2} = TK_{T_3} - TK_{T_2} - \int_{T_2}^{T_{F_2}} f_3(t)dt - \int_{T_{F_2}+3}^{T_3} f_4(t)dt \qquad \text{(Equation 2)}$$

where TK_{T_3} is the amount of thermokarst observed at T_3 (Figure S5). $f_3(t)$ and $f_4(t)$ correspond to thermokarst rates between T_2 and the repeat burn, and between the repeat burn and T_3, respectively (Figure S5). Similar to $f_2(t)$, $f_3(t)$ corresponds to postfire thermokarst rates following the initial burn. In contrast, $f_4(t)$ is likely subjected to the influence of both the initial and the repeat burns (Figure S5). We approximated $f_4(t)$ with three scenarios assuming a different contribution of each burn. Scenario 1 assumes no impact of the repeat burn, and $f_4(t)$ depends solely on the legacy of the initial burn. Alternatively, scenario 2 assumes no impact of the initial burn, and $f_4(t)$ is dictated entirely by the impacts of the repeat burn. Scenario 3 assumes contributions of both burns, and $f_4(t)$ is computed as the sum of scenarios 1 and 2.

Modeling thermokarst rate

We modeled thermokarst rates using BRT algorithm fitted in R v3.6.1 (with package *gbm*[68]). The BRT is a machine learning approach that integrates the strengths of regression trees and boosting to form an ensemble model with optimized predictive performance.[69] We chose BRT on account of (1) its success in describing patterns and making predictions in a range of ecological problems,[70–72] (2) its sophistication in managing high-order interactions and collinearity of predictors, and (3) its capacity in handling missing data, outliers, and different types of inputs. Further details of the theory and practice of BRT can be found in Elith et al.[69]

We selected 24 candidate predictors (Table S2) for thermokarst, informed by previous studies[3,6,7,13,15,23,24,56,61,73–77] and the findings of the current study. These explanatory variables can be broadly categorized into three groups: (1) meteorological or phenological variables ($n = 14$), including temperature and precipitation, (2) topographical or geological variables ($n = 8$), such as permafrost distribution and landcover, and (3) disturbance variables ($n = 2$): fire severity and YSF. We obtained datasets of variables in the first two categories from geospatial databases (Table S2). The fire severity dataset was derived from the MTBS archive (https://www.mtbs.gov/) and Chen et al.[36] The YSF value is assigned to each observation based on its temporal distance from fire occurrence.[31] For unburned observations in the NOAT, their YSF is approximated as the regional mean FRI, computed with the equation given by Johnson and Gutsell:[78]

$$FRI = \frac{t}{\sum_{i=1}^{n} \frac{a_i}{A}} \quad \text{(Equation 3)}$$

where t accounts for the time span of fire observation, n is the number of fires, a_i represents the area burned by fire i, and A refers to the vegetated area of the region.

We divided our observations into training and validation datasets in the ratio of 80% to 20%. We initially fitted the model on the training data between the whole set of candidate predictors and thermokarst rate, and then removed non-significant variables in a stepwise fashion following the principle of maximum parsimony and minimizing cross-dependent/cross-correlative variables.[72] The regularization parameters of the model were tested before being fixed at the optimal bag fraction of 0.75, learning rate of 0.0005, and tree complexity of 10, which resulted in the number of trees >5,000. Model performance was evaluated using the default 10-fold cross-validation (Figure S7). Six variables (YSF, PP, MSAT, TPI, FSS, and LOGS) that demonstrate the heaviest influence (relative influence >5%) on thermokarst rates were retained in the final model (Figure S6), which achieved an explanatory power of R^2 = 0.73 (10-CV = 0.69 ± 0.01, $p < 0.001$; Figure S7). The model was further validated by the independent validation dataset (Figure S7), confirming its strength in reproducing the observed thermokarst patterns in the NOAT ($p < 0.001$, $R^2 = 0.7$).

Model extrapolation and validation

We extrapolated our findings in the NOAT using the BRT model generated above to the northern Alaskan tundra biome (>64°N), which comprises 2.6 × 10^5 km^2 of land surface (excluding lakes, glaciers, ice sheets, and barren lands) and consists of six tundra ecoregions (i.e., Arctic Coastal Plain, Brooks Range Foothills, Brooks Range, Kotzebue Sound Lowlands, NOAT, and Seward Peninsula). We conducted a pair of model runs allowing (fireRun) and prohibiting (nofireRun) fire occurrence as a means to isolating the contribution of tundra fire to overall thermokarst formation. For both scenarios, we run the model on a 1-km^2 grid cell at an annual time step spanning 1950–2015 with a 10-year spin-up to adjust the initial YSF. The YSF value of a given cell in a given year was calculated from the AICC fire observation (burned) or as regional mean FRI (unburned) (Equation 3).

For the fireRun, we converted annual AICC fire polygons (1950–2015) to a multi-layer raster stack (cell size = 1 km^2) so that each layer records the loci of burned (value of 1) and unburned (value of 0) cells in a given year. The same raster stack was created for the nofireRun except for assigning all cells to 0 to turn off fire occurrence. Model spin-up of the two simulations was forced with an identical input dataset. For the spin-up period (1940–1949) with no reliable fire observation data, we assumed it had a fire regime similar to the mean fire regime during 1950–2015. Thus, for a specific ecoregion, the annual fire occurrence dataset of spin-up was created by randomly selecting pixels to burn an area equivalent to the average annual area burned between 1950 and 2015. To avoid repeated sampling of burned cells, only cells not burned in previous years were selected. The fire occurrence datasets spanning 1940–2015 were then transformed to annual YSF forcing. In brief, all cells were initiated as unburned. The YSF value was updated annually according to the fire occurrence dataset: YSF remains unchanged unless fires occur, in which case YSF of the cell upgrades to 1. For every year past fire, YSF increases by 1 until the next fire occurs and its value returns back to 1, repeating the cycle. The contribution of fire disturbance to overall thermokarst formation was then computed as the difference between the fireRun and the nofireRun. To further isolate the contribution of climate change to remaining thermokarst formation, an additional model run prohibiting fire disturbance and forced with linearly detrended climate inputs (MSAT and LOGS)[79,80] was conducted, and the result was subtracted from the nofireRun to calculate thermokarst attributable to changing climate.

Model output of the fireRun (Figure 5) was validated by 14 validation sites (Table S3) and by published data (n = 14) from northern Alaskan tundra (refs.[3,17,19,38]) (Figure 1). Two sites were randomly placed in each of the five northern Alaskan tundra ecoregions outside the NOAT (Table S3), one in burned and one in unburned areas, except for the Arctic Coastal Plain, where both sites were placed in unburned tundra due to the paucity of wildfires. Additionally, we set up four study sites in the Anaktuvuk River Fire to evaluate model performance in extreme settings (e.g., ice-rich tundra burned in extreme severity[26]): two in ice-rich yedoma deposits (one in burned and one in unburned) and two in non-yedoma deposits (one in burned and one in unburned) (Table S3). We analyzed thermokarst rate for each validation site using the same approach described earlier (Figure S2). The published data used for validation were either collected by *in situ* measurements or by optical-based remote sensing.

Statistical analyses

We analyzed the difference in immediate thermokarst formation between four fire severity regimes and three surficial geology types using an unbalanced two-way analysis of variance (ANOVA). The independent factors were specified as fire severity and surficial geology. All pairwise comparisons were conducted using the Games-Howell post hoc tests for datasets with unequal variances and unequal sample sizes. The datasets were checked for normality using Shapiro-Wilk test and transformed prior to statistical analysis. To account for the repeated measure in our study for long-term thermokarst response, the mixed-design ANOVA was applied to determine the differences between time intervals and between fire severity regimes, where the within-subjects factor is specified as time intervals and the between-subjects factor is fire severity regime. The degrees of freedom were adjusted using the Greenhouse-Geisser adjustment to meet the sphericity of the covariance matrix assumption. We performed a two-tailed Student's t test to compare pulse thermokarst growth between the initial burns and the repeat burns. Linear regression analysis was used to assess the relationship between FRI and pulse thermokarst growth by repeat burn. All statistical analyses were conducted in R v3.6.1, and differences were considered significant at a level of $p < 0.05$.

SUPPLEMENTAL INFORMATION

Supplemental information can be found online at https://doi.org/10.1016/j.oneear.2021.11.011.

ACKNOWLEDGMENTS

Funding for this research was provided by the NSF (1023477 and 1636476 to F.S.H and 1928048 to M.J.L). We are grateful for the geospatial support provided for this work by the Polar Geospatial Center under NSF PLR awards 1043681 and 1559691. Any use of trade, firm, or product names is for descriptive purposes only and does not imply endorsement by the US Government.

AUTHOR CONTRIBUTIONS

Conceptualization, Y.C., M.J.L., and F.S.H.; methodology, Y.C. and M.J.L.; investigation, Y.C.; data curation, Y.C., M.J.L., and F.S.H.; writing – original draft, Y.C.; writing – review & editing, Y.C., M.J.L., F.S.H., B.M.J., and G.V.F.; visualization, Y.C.; validation, Y.C., M.J.L., B.M.J., and G.V.F.; supervision, F.S.H. funding acquisition, M.J.L. and F.S.H.

DECLARATION OF INTERESTS

The authors declare no competing interests.

Received: July 2, 2021
Revised: October 28, 2021
Accepted: November 23, 2021
Published: December 9, 2021

REFERENCES

1. Obu, J., Westermann, S., Bartsch, A., Berdnikov, N., Christiansen, H.H., Dashtseren, A., Delaloye, R., Elberling, B., Etzelmüller, B., Kholodov, A., et al. (2019). Northern Hemisphere permafrost map based on TTOP modelling for 2000–2016 at 1 km2 scale. Earth Sci. Rev. *193*, 299–316.
2. Meredith, M., Sommerkorn, M., Cassotta, S., Derksen, C., Ekaykin, A., Hollowed, A., et al. (2019). Polar regions. In IPCC Special Report on the Ocean and Cryosphere in a Changing Climate, H.O. Pörtner, D.C. Roberts, V. Masson-Delmotte, P. Zhai, M. Tignor, and E. Poloczanska, et al., eds. (Cambridge University Press), pp. 215–260.

3. Jorgenson, M.T., Shur, Y.L., and Pullman, E.R. (2006). Abrupt increase in permafrost degradation in Arctic Alaska. Geophys. Res. Lett. *33*, 2–5.
4. Kokelj, S.V., Tunnicliffe, J., Lacelle, D., Lantz, T.C., Chin, K.S., and Fraser, R. (2015). Increased precipitation drives mega slump development and destabilization of ice-rich permafrost terrain, northwestern Canada. Glob. Planet. Change *129*, 56–68.
5. Holloway, J.E., Lewkowicz, A.G., Douglas, T.A., Li, X., Turetsky, M.R., Baltzer, J.L., and Jin, H. (2020). Impact of wildfire on permafrost landscapes: a review of recent advances and future prospects. Permafr. Periglac. Process. *31*, 371–382.
6. Lara, M.J., Chipman, M.L., and Hu, F.S. (2019). Automated detection of thermoerosion in permafrost ecosystems using temporally dense Landsat image stacks. Remote Sens. Environ. *221*, 462–473.
7. Jones, B.M., Grosse, G., Arp, C.D., Miller, E., Liu, L., Hayes, D.J., and Larsen, C.F. (2015). Recent Arctic tundra fire initiates widespread thermokarst development. Sci. Rep. *5*, 1–13.
8. Nitzbon, J., Westermann, S., Langer, M., Martin, L.C.P., Strauss, J., Laboor, S., and Boike, J. (2020). Fast response of cold ice-rich permafrost in northeast Siberia to a warming climate. Nat. Commun. *11*, 1–11.
9. Turetsky, M.R., Abbott, B.W., Jones, M.C., Anthony, K.W., Olefeldt, D., Schuur, E.A.G., Grosse, G., Kuhry, P., Hugelius, G., Koven, C., et al. (2020). Carbon release through abrupt permafrost thaw. Nat. Geosci. *13*, 138–143.
10. Abbott, B.W., and Jones, J.B. (2015). Permafrost collapse alters soil carbon stocks, respiration, CH_4, and N_2O in upland tundra. Glob. Chang. Biol. *21*, 4570–4587.
11. Schuur, E.A.G., Bockheim, J., Canadell, J.G., Euskirchen, E., Field, C.B., Goryachkin, S.V., Hagemann, S., Kuhry, P., Lafleur, P.M., Lee, H., et al. (2008). Vulnerability of permafrost carbon to climate change: implications for the global carbon cycle. Bioscience *58*, 701–714.
12. Turetsky, M.R., Jones, M.C., Walter Anthony, K., Olefeldt, D., Schuur, E.A.G., Koven, C., Mcguire, A.D., and Grosse, G. (2019). Permafrost collapse is accelerating carbon release. Nature *569*, 32–34.
13. Jorgenson, M.T., Romanovsky, V., Harden, J., Shur, Y., O'Donnell, J., Schuur, E.A.G., Kanevskiy, M., and Marchenko, S. (2010). Resilience and vulnerability of permafrost to climate change. Can. J. For. Res. *40*, 1219–1236.
14. Osterkamp, T.E., Jorgenson, M.T., Schuur, E.A.G., Shur, Y.L., Kanevskiy, M.Z., Vogel, J.G., and Tumskoy, V.E. (2009). Physical and ecological changes associated with warming permafrost and thermokarst in Interior Alaska. Permafr. Periglac. Process. *20*, 235–256.
15. Kokelj, S.V., and Jorgenson, M.T. (2013). Advances in thermokarst research. Permafr. Periglac. Process. *24*, 108–119.
16. O'Donnell, J.A., Jorgenson, M.T., Harden, J.W., McGuire, A.D., Kanevskiy, M.Z., and Wickland, K.P. (2012). The effects of permafrost thaw on soil hydrologic, thermal, and carbon dynamics in an alaskan peatland. Ecosystems *15*, 213–229.
17. Jorgenson, M.T., Kanevskiy, M., Shur, Y., Moskalenko, N., Brown, D.R.N., Wickland, K., Striegl, R., and Koch, J. (2015). Role of ground ice dynamics and ecological feedbacks in recent ice wedge degradation and stabilization. J. Geophys. Res. Earth Surf. *120*, 2280–2297.
18. Schuur, E.A.G., McGuire, A.D., Schädel, C., Grosse, G., Harden, J.W., Hayes, D.J., Hugelius, G., Koven, C.D., Kuhry, P., Lawrence, D.M., et al. (2015). Climate change and the permafrost carbon feedback. Nature *520*, 171–179.
19. Frost, G.V., Christopherson, T., Jorgenson, M.T., Liljedahl, A.K., Macander, M.J., Walker, D.A., and Wells, A.F. (2018). Regional patterns and asynchronous onset of ice-wedge degradation since the mid-20th century in Arctic Alaska. Remote Sens *10*, 1312.
20. Shur, Y.L., and Jorgenson, M.T. (2007). Patterns of permafrost formation and degradation in relation to climate and ecosystems. Permafr. Periglac. Process. *18*, 7–19.
21. Olefeldt, D., Goswami, S., Grosse, G., Hayes, D., Hugelius, G., Kuhry, P., Mcguire, A.D., Romanovsky, V.E., Sannel, A.B.K., Schuur, E.A.G., et al. (2016). Circumpolar distribution and carbon storage of thermokarst landscapes. Nat. Commun. *7*, 1–11.
22. Yanagiya, K., and Furuya, M. (2020). Post-wildfire surface deformation near batagay, eastern Siberia, detected by L-band and C-band InSAR. J. Geophys. Res. Earth Surf. *125*, 1–18.
23. Jorgenson, M.T., and Osterkamp, T.E. (2005). Response of boreal ecosystems to varying modes of permafrost degradation. Can. J. For. Res. *35*, 2100–2111.
24. Jorgenson, M., Harden, J., Kanevskiy, M., O'Donnell, J., Wickland, K., Ewing, S., Manies, K., Zhuang, Q., Shur, Y., Striegl, R., et al. (2013). Reorganization of vegetation, hydrology and soil carbon after permafrost degradation across heterogeneous boreal landscapes. Environ. Res. Lett. *8*, 035017.
25. Chen, J., Wu, Y., O'Connor, M., Cardenas, M.B., Schaefer, K., Michaelides, R., and Kling, G. (2020). Active layer freeze-thaw and water storage dynamics in permafrost environments inferred from InSAR. Remote Sens. Environ. *248*, 112007.
26. Mack, M.C., Bret-Harte, M.S., Hollingsworth, T.N., Jandt, R.R., Schuur, E.A.G., Shaver, G.R., and Verbyla, D.L. (2011). Carbon loss from an unprecedented Arctic tundra wildfire. Nature *475*, 489–492.
27. Higuera, P.E., Chipman, M.L., Barnes, J.L., Urban, M.A., and Hu, F.S. (2011). Variability of tundra fire regimes in Arctic Alaska: millennial-scale patterns and ecological implications. Ecol. Appl. *21*, 3211–3226.
28. Hu, F.S., Higuera, P.E., Duffy, P., Chipman, M.L., Rocha, A.V., Young, A.M., Kelly, R., and Dietze, M.C. (2015). Arctic tundra fires: natural variability and responses to climate change. Front. Ecol. Environ. *13*, 369–377.
29. Sousanes, P.J., and Hill, K. (2017). Climate Summary for the Arctic Parks. Arctic Inventory and Monitoring Network. Natural Resource Report, NPS/ARCN/NRR-2017/1574 (National Park Service).
30. Rocha, A.V., Loranty, M.M., Higuera, P.E., MacK, M.C., Hu, F.S., Jones, B.M., Breen, A.L., Rastetter, E.B., Goetz, S.J., and Shaver, G.R. (2012). The footprint of Alaskan tundra fires during the past half-century: implications for surface properties and radiative forcing. Environ. Res. Lett. *7*, 044039.
31. AICC 1950-2020 Alaska Interagency Coordination Center (2021). https://fire.ak.blm.gov/. Accessed January 20, 2021
32. Moritz, M.A., Parisien, M.A., Batllori, E., Krawchuk, M.A., Van Dorn, J., Ganz, D.J., and Hayhoe, K. (2012). Climate change and disruptions to global fire activity. Ecosphere *3*, 49.
33. Danielson, J.J., and Gesch, D.B. (2011). Global Multi-Resolution Terrain Elevation Data 2010 (GMTED2010). Open-File Report 2011–1073 (U.S. Department of the Interior, U.S. Geological Survey.).
34. Hamilton, T.D. (2010). Surficial Geologic Map of the Noatak National Preserve, Alaska (U.S. Geological Survey Scientific Investigations Map), p. 3036.
35. Jorgenson, M.T., Kanevskiy, M., Shur, Y., Grunblatt, J., Ping, C.L., and Michaelson, G. (2014). Permafrost Database Development, Characterization, and Mapping for Northern Alaska (U.S. Fish and Wildlife Service).
36. Chen, Y., Lara, M.J., and Hu, F.S. (2020). A robust visible near-infrared index for fire severity mapping in Arctic tundra ecosystems. ISPRS J. Photogramm. Remote Sens. *159*, 101–113.
37. Chen, Y., Hu, F.S., and Lara, M.J. (2021). Divergent shrub-cover responses driven by climate, wildfire, and permafrost interactions in Arctic tundra ecosystems. Glob. Chang. Biol. *27*, 652–663.
38. Raynolds, M.K., Walker, D.A., Ambrosius, K.J., Brown, J., Everett, K.R., Kanevskiy, M., Kofinas, G.P., Romanovsky, V.E., Shur, Y., and Webber, P.J. (2014). Cumulative geoecological effects of 62 years of infrastructure and climate change in ice-rich permafrost landscapes, Prudhoe Bay Oilfield, Alaska. Glob. Chang. Biol. *20*, 1211–1224.
39. Rocha, A.V., and Shaver, G.R. (2011). Postfire energy exchange in arctic tundra: the importance and climatic implications of burn severity. Glob. Chang. Biol. *17*, 2831–2841.

40. Roland, C.A., Schmidt, J.H., Winder, S.G., Stehn, S.E., and Nicklen, E.F. (2019). Regional variation in interior Alaskan boreal forests is driven by fire disturbance, topography, and climate. Ecol. Monogr. *89*, 1–34.

41. Neumann, R.B., Moorberg, C.J., Lundquist, J.D., Turner, J.C., Waldrop, M.P., McFarland, J.W., Euskirchen, E.S., Edgar, C.W., and Turetsky, M.R. (2019). Warming effects of spring rainfall increase methane emissions from thawing permafrost. Geophys. Res. Lett. *46*, 1393–1401.

42. Gibson, C.M., Chasmer, L.E., Thompson, D.K., Quinton, W.L., Flannigan, M.D., and Olefeldt, D. (2018). Wildfire as a major driver of recent permafrost thaw in boreal peatlands. Nat. Commun. *9*, 3041.

43. Bret-Harte, M.S., Mack, M.C., Shaver, G.R., Huebner, D.C., Johnston, M., Mojica, C.A., Pizano, C., and Reiskind, J.A. (2013). The response of Arctic vegetation and soils following an unusually severe tundra fire. Philos. Trans. R. Soc. B Biol. Sci. *368*, 20120490.

44. He, J., Loboda, T.V., Jenkins, L., and Chen, D. (2019). Mapping fractional cover of major fuel type components across Alaskan tundra. Remote Sens. Environ. *232*, 111324.

45. Serreze, M.C., and Barry, R.G. (2011). Processes and impacts of Arctic amplification: a research synthesis. Glob. Planet. Change *77*, 85–96.

46. Farquharson, L.M., Romanovsky, V.E., Cable, W.L., Walker, D.A., Kokelj, S.V., and Nicolsky, D. (2019). Climate change drives widespread and rapid thermokarst development in very cold permafrost in the Canadian high arctic. Geophys. Res. Lett. *46*, 6681–6689.

47. Nitze, I., Grosse, G., Jones, B.M., Romanovsky, V.E., and Boike, J. (2018). Remote sensing quantifies widespread abundance of permafrost region disturbances across the Arctic and Subarctic. Nat. Commun. *9*, 1–11.

48. Brown, D., Jorgenson, M.T., Douglas, T., and Ruess, R. (2015). Interactions of fire and climate exacerbate permafrost degradation in alaskan lowland forests. J. Geophys. Res. Biogeosci. *120*, 1619–1637.

49. Jorgenson, M.T., Racine, C.H., Walters, J.C., and Osterkamp, T.E. (2001). Permafrost degradation and ecological changes associated with a warming climate in central Alaska. Clim. Change *48*, 551–579.

50. McCarty, J.L., Smith, T.E.L., and Turetsky, M.R. (2020). Arctic fires re-emerging. Nat. Geosci. *13*, 658–660.

51. Jones, B.M., Farquharson, L.M., Baughman, C.A., Buzard, R.M., Arp, C.D., Grosse, G., Bull, D.L., Günther, F., Nitze, I., Urban, F., et al. (2018). A decade of remotely sensed observations highlight complex processes linked to coastal permafrost bluff erosion in the Arctic. Environ. Res. Lett. *13*, 115001.

52. Lewkowicz, A.G., and Way, R.G. (2019). Extremes of summer climate trigger thousands of thermokarst landslides in a High Arctic environment. Nat. Commun. *10*, 1–11.

53. Luo, J., Niu, F., Lin, Z., Liu, M., and Yin, G. (2019). Recent acceleration of thaw slumping in permafrost terrain of Qinghai-Tibet Plateau: an example from the Beiluhe Region. Geomorphology *341*, 79–85.

54. Rudy, A.C.A., Lamoureux, S.F., Kokelj, S.V., Smith, I.R., and England, J.H. (2017). Accelerating thermokarst transforms ice-cored terrain triggering a downstream cascade to the ocean. Geophys. Res. Lett. *44*, 11080–11087.

55. Segal, R.A., Lantz, T.C., and Kokelj, S.V. (2016). Acceleration of thaw slump activity in glaciated landscapes of the Western Canadian Arctic. Environ. Res. Lett. *11*, 034025.

56. Liljedahl, A.K., Boike, J., Daanen, R.P., Fedorov, A.N., Frost, G.V., Grosse, G., Hinzman, L.D., Iijma, Y., Jorgenson, J.C., Matveyeva, N., et al. (2016). Pan-Arctic ice-wedge degradation in warming permafrost and its influence on tundra hydrology. Nat. Geosci. *9*, 312–318.

57. Wild, B., Andersson, A., Bröder, L., Vonk, J., Hugelius, G., McClelland, J.W., Song, W., Raymond, P.A., and Gustafsson, Ö. (2019). Rivers across the Siberian Arctic unearth the patterns of carbon release from thawing permafrost. Proc. Natl. Acad. Sci. U S A *116*, 10280–10285.

58. Hugelius, G., Loisel, J., Chadburn, S., Jackson, R.B., Jones, M., MacDonald, G., Marushchak, M., Olefeldt, D., Packalen, M., Siewert, M.B., et al. (2020). Large stocks of peatland carbon and nitrogen are vulnerable to permafrost thaw. Proc. Natl. Acad. Sci. U S A *117*, 20438–20446.

59. McGuire, A.D., Lawrence, D.M., Koven, C., Clein, J.S., Burke, E., Chen, G., Jafarov, E., MacDougall, A.H., Marchenko, S., Nicolsky, D., et al. (2018). Dependence of the evolution of carbon dynamics in the northern permafrost region on the trajectory of climate change. Proc. Natl. Acad. Sci. U S A *115*, 3882–3887.

60. Raynolds, M.K., Breen, A.L., and Walker, D.A. (2017). Land Cover and Ecosystem Map Collection for Northern Alaska (ORNL DAAC).

61. Jorgenson, M.T., Roth, J.E., Miller, P.F., Macander, M.J., Duffy, M.S., Wells, A.F., Frost, G.V., and Pullman, E.R. (2009). An Ecological Land Survey and Landcover Map of the Arctic Network. Natural Resource Technical Report NPS/ARCN/NRTR-2009/270 (National Park Service, U.S. Department of the Interior).

62. Jorgenson, M.T., and Grunblatt, J. (2013). Landscape-Level Ecological Mapping of Northern Alaska and Field Site Photography. Final Report Prepared for: Arctic Landscape Conservation Cooperative (U.S. Fish and Wildlife Service).

63. Necsoiu, M., Dinwiddie, C.L., Walter, G.R., Larsen, A., and Stothoff, S.A. (2013). Multi-temporal image analysis of historical aerial photographs and recent satellite imagery reveals evolution of water body surface area and polygonal terrain morphology in Kobuk Valley National Park, Alaska. Environ. Res. Lett. *8*, 025007.

64. Kokelj, S.V., Lacelle, D., Lantz, T.C., Tunnicliffe, J., Malone, L., Clark, I.D., and Chin, K.S. (2013). Thawing of massive ground ice in mega slumps drives increases in stream sediment and solute flux across a range of watershed scales. J. Geophys. Res. Earth Surf. *118*, 681–692.

65. Loboda, T.V., French, N.H.F., Hight-Harf, C., Jenkins, L., and Miller, M.E. (2013). Mapping fire extent and burn severity in Alaskan tussock tundra: an analysis of the spectral response of tundra vegetation to wildland fire. Remote Sens. Environ. *134*, 194–209.

66. Baltzer, J.L., Veness, T., Chasmer, L.E., Sniderhan, A.E., and Quinton, W.L. (2014). Forests on thawing permafrost: fragmentation, edge effects, and net forest loss. Glob. Chang. Biol. *20*, 824–834.

67. Lara, M.J., Genet, H., Mcguire, A.D., Euskirchen, E.S., Zhang, Y., Brown, D.R.N., Jorgenson, M.T., Romanovsky, V., Breen, A., and Bolton, W.R. (2016). Thermokarst rates intensify due to climate change and forest fragmentation in an Alaskan boreal forest lowland. Glob. Chang. Biol. *22*, 816–829.

68. Ridgeway, G. (2019). Generalized Boosted Models: a guide to the gbm package. R. Packag. Vignette *1*, 1–12.

69. Elith, J., Leathwick, J.R., and Hastie, T. (2008). A working guide to boosted regression trees. J. Anim. Ecol. *77*, 802–813.

70. Maino, J.L., Umina, P.A., and Hoffmann, A.A. (2018). Climate contributes to the evolution of pesticide resistance. Glob. Ecol. Biogeogr. *27*, 223–232.

71. Mayer, D.G., Chandra, K.A., and Burnett, J.R. (2019). Improved crop forecasts for the Australian macadamia industry from ensemble models. Agric. Syst. *173*, 519–523.

72. Natali, S.M., Watts, J.D., Rogers, B.M., Potter, S., Ludwig, S.M., Selbmann, A.K., Sullivan, P.F., Abbott, B.W., Arndt, K.A., Birch, L., et al. (2019). Large loss of CO_2 in winter observed across the northern permafrost region. Nat. Clim. Chang. *9*, 852–857.

73. Kokelj, S.V., Lantz, T.C., Wolfe, S.A., Kanigan, J.C., Morse, P.D., Coutts, R., Molina-Giraldo, N., and Burn, C.R. (2014). Distribution and activity of ice wedges across the forest-tundra transition, western Arctic Canada. J. Geophys. Res. Earth Surf. *119*, 2032–2047.

74. Riordan, B., Verbyla, D., and McGuire, A.D. (2006). Shrinking ponds in subarctic Alaska based on 1950-2002 remotely sensed images. J. Geophys. Res. Biogeosci. *111*.

75. Roach, J., Griffith, B., Verbyla, D., and Jones, J. (2011). Mechanisms influencing changes in lake area in Alaskan boreal forest. Glob. Chang. Biol. *17*, 2567–2583.

76. Smith, L.C., Sheng, Y., MacDonald, G.M., and Hinzman, L.D. (2005). Atmospheric science: disappearing arctic lakes. Science *308*, 1429.

77. Biskaborn, B.K., Smith, S.L., Noetzli, J., Matthes, H., Vieira, G., Streletskiy, D.A., Schoeneich, P., Romanovsky, V.E., Lewkowicz, A.G., Abramov, A., et al. (2019). Permafrost is warming at a global scale. Nat. Commun. *10*, 264.

78. Johnson, E.A., and Gutsell, S.L. (1994). Fire frequency models, methods and interpretations. Adv. Ecol. Res. *25*, 239–287.

79. Berner, L.T., Massey, R., Jantz, P., Forbes, B.C., Macias-Fauria, M., Myers-Smith, I., Kumpula, T., Gauthier, G., Andreu-Hayles, L., Gaglioti, B.V., et al. (2020). Summer warming explains widespread but not uniform greening in the Arctic tundra biome. Nat. Commun. *11*, 4621.

80. Burrell, A.L., Evans, J.P., and De Kauwe, M.G. (2020). Anthropogenic climate change has driven over 5 million km2 of drylands towards desertification. Nat. Commun. *11*, 1–11.